



Inclusion orientation dependent flaking process in rolling contact fatigue observed by laminography using ultrabright synchrotron radiation X-ray

Nakai, Yoshikazu ; Shiozawa, Daiki ; Kikuchi, Shoichi ; Saito, Hitoshi ; Nishina, Takashi ; Kobayashi, Hiroshi ; Makino, Taizo ; Neishi, ...

(Citation)

Fatigue & Fracture of Engineering Materials & Structures, 45(8):2200-2214

(Issue Date)

2022-08-01

(Resource Type)

journal article

(Version)

Accepted Manuscript

(Rights)

This is the peer reviewed version of the following article: [Nakai, Y, Shiozawa, D, Kikuchi, S, et al. Inclusion orientation dependent flaking process in rolling contact fatigue observed by laminography using ultrabright synchrotron radiation X-ray. Fatigue Fract Eng Mater Struct. 2022; 45(8): 2200-2214.], which has been published i...

(URL)

<https://hdl.handle.net/20.500.14094/0100476805>



Inclusion orientation dependent flaking process in rolling contact fatigue observed by laminography using ultrabright synchrotron radiation X-ray

Yoshikazu Nakai* and Daiki Shiozawa

Department of Mechanical Engineering, Kobe University

1-1, Rokkodai, Nada, Kobe 657-8501, Japan

* Corresponding author, nakai@mech.kobe-u.ac.jp

Shoichi Kikuchi

Department of Mechanical Engineering, Shizuoka University

3-5-1, Johoku, Naka, Hamamatsu 432-8561, Japan

Hitoshi Saito, Takashi Nishina, and Hiroshi Kobayashi

Department of Mechanical Engineering, Kobe University

1-1, Rokkodai, Nada, Kobe 657-8501, Japan

Taizo Makino

Nippon Steel Corporation, Research & Development, 1-8, Fuso, Amagasaki 660-0891, Japan

Yutaka Neishi

Nippon Steel Corporation, Research & Development, 20-1 Shintomi, Futtsu 293-8511, Japan

Key words: Rolling contact fatigue; Crack path; Image processing; Inclusions; Finite elements

Abstract

The formation and propagation of cracks in rolling contact fatigue were observed by synchrotron radiation computed laminography, and the effect of stringer-type inclusion orientation was examined. For longitudinal inclusions, cracks started forming at their tips. After cracks propagated toward the rolling direction, a longitudinal crack was kinked simultaneously at both its tips, and propagated toward the direction perpendicular to the rolling direction to form lateral cracks. After kinking, horizontal cracks were formed from the deepest point of a lateral crack, leading to flaking. On the other hand, for specimens with lateral inclusions, cracks propagated to the lateral direction without the formation of longitudinal cracks. Since the propagation life of lateral cracks and that of horizontal cracks were unrelated to the inclusion orientation, the rolling contact fatigue life of specimens with longitudinal inclusions was considerably longer than that of specimens with lateral inclusions.

1 INTRODUCTION

Rolling contact fatigue (RCF) is a crucial factor for mechanical elements subjected to rolling contact. To extend the service life of machinery subjected to rolling contact, such as bearings, gears, wheels, and rails, it is necessary to investigate the RCF mechanism and mechanics. In gears, wheels, and rails, macroscopic slips play an important role in the RCF damage process,^{1, 2} where strong friction (tangential force) is induced on the rolling contact surface, and surface cracks start to form and propagate obliquely from the surface and eventually grow to form RCF damage called shelling³ or pitting.² In contrast, bearings are generally applied under pure rolling contact and oil lubrication with weak friction without macroscopic slips. In this case, it has been believed that cracks start to form beneath the surface, leading to RCF damage called flaking.

The above-described difference was attributed to the stress intensity factor range of cracks below the surface,⁴ or shear stress distribution.⁵ Not only the initiation site, but also the initiation mechanism of cracks differs in RCF between strong and weak friction, *i.e.*, shelling/pitting and flaking.⁶ The mechanics of shelling/pitting was analyzed on the basis of fracture mechanics^{1,7,8} and on the basis of shear stress calculated by finite element (FE) analysis.^{9–11} Microstructural alterations of the matrix beneath the surface have been considered as important causes of RCF without friction under oil lubrication. Such alterations may be a dark etching area (DEA),^{12,13} dark etching constituent (DEC),¹² dark etching region (DER),^{12,14} and martensite transformation from retained austenite,¹³ which occur in high-stress regions under the ball track. As the number of fatigue cycles increases, characteristic microstructures appear, such as the white band (WB),^{12,13} which is type a of shear band, the white etching band (WEB),^{12,14} white etching area (WEA),^{12, 15–19} white etching cracks (WEC),^{14,16} brown etching layer (BEL),¹⁵ and butterfly cracks.¹⁷ The WEA was found to be composed of ultrafine nanocrystalline ferrite grains, voids, and spherical carbides, as observed by transmission electron microscopy.^{16–18} Hiraoka et al.²⁰ observed that WEA occurred after microcrack initiation. Martin et al.²¹ examined microstructural alterations, which develop with cyclic stressing under rolling contact, and attempted to define their nature and formation mechanisms. In many cases, ‘winglike’ structural alterations, commonly called ‘butterflies’, were microcracks associated with inclusions.^{19,22,23} Evans et al.¹⁷ conducted 3D reconstruction of the butterfly wing by cross-sectional focused ion beam (FIB)

milling with an average slice thickness of 350 nm. Although numerous studies have been conducted on microstructural alterations, the process from microstructural alteration to flaking has not yet been clarified.

On the other hand, Kanetani and Ushida reported that cracks usually started forming from non-metallic inclusions rather than WBs.¹² The detrimental effect of inclusions in terms of RCF has been discussed,^{17,19,20,24–41} and it has been found that the size, shape, orientation, location, composition of inclusions, and interface conditions between inclusions and the surrounding matrix can be considered to be factors affecting the RCF life. The refinement of inclusions contributes to improving the RCF strength. Chen et al.²⁵ investigated how the type, size, and location of inclusions control crack initiation in the RCF test. Lewis and Tomkins³⁰ applied the root-area parameter model to predict microcrack propagation from inclusions. Hashimoto et al.²⁹ concluded that smaller inclusions, high interfacial strength, and smaller differences in Young's modulus between an inclusion and the surrounding matrix led to longer RCF life.

Most of the above-mentioned studies focused on internal inclusions. It has been recognized that flaking starts from inclusions beneath the surface where the ball track is located and the shear stress is greatest, and the cracks grow from them toward the surface.^{39,40} On the other hand, Nagao et al.²⁶ reported that the mechanism depended on the shape of inclusions, *i.e.*, horizontal cracks were formed from spherical inclusions, whereas lateral cracks were first formed from stringer-type inclusions whose long axis was perpendicular to the rolling direction (lateral inclusion). In this case, horizontal cracks were formed after the formation of lateral cracks. The formation and propagation of lateral cracks were considered to be controlled by the normal stress, whereas the propagation of horizontal cracks was controlled by the shear stress. Tsuchida and Tamura³² observed that horizontal cracks were formed from spherical inclusions, however; they considered that crack initiation was controlled by the normal stress. These observations were conducted by terminating the RCF test before flaking occurred and cutting the specimens. Therefore, sequential observations of the initiation and propagation of the lateral crack and horizontal crack, and the flaking process have not been conducted.

Alley and Neu⁴¹ analyzed the effect of the orientation on lateral inclusions. Their analysis was based on the stress beneath the surface, which was calculated by FE analysis. They found that RCF strength is lowest for inclusions with the orientation of 45°, where the orientation is defined as the complementary angle between the long axis of an inclusion and the normal of the surface, and the RCF strength is highest for the orientation of 0° (vertical inclusion). On the other hand, Allison and Pandkar⁴² evaluated the RCF limit of longitudinal and lateral inclusions using the maximum orthogonal shear stress beneath the surface calculated by FE analysis, and concluded that the effects of the inclusion orientation and geometry on the RCF limit were minor.

Another subject concerning RCF is the failure probability, because the basic rating life of bearings, L10 life, is defined as the RCF life where 90% of specimens fail under identical loading and lubrication conditions. Using the orthogonal shear stress calculated by FE analysis and using the *S–N* curve obtained by the conventional fatigue test, the various research groups evaluated fracture probability in RCF, where the scatter of RCF life values attributed to the scatter in the conventional fatigue test^{43–46} or crystalline anisotropy.⁴⁷ Kerrigan et al.²⁷ and Unigame²⁸ reported that the inclusion distribution obtained from the statistics of extreme values can be used to predict L10 life.

81 Since the phenomena causing RCF have been considered to occur beneath the surface,
82 observations have been conducted destructively by cutting specimens. Thus, successive observations
83 of RCF have not been conducted. Naeimi et al.⁴⁸ and Jessop et al.⁴⁹ observed macro RCF-cracks
84 formed in rails using an industrial computed tomography (CT) scanner with a resolution of around 1
85 mm; however, this resolution is not sufficient for observing microcracks. On the other hand, 3D
86 imaging of materials with submicron resolution can be accomplished by using ultra-bright
87 synchrotron radiation X-rays, called SR- μ CT. By SR- μ CT imaging, we successfully observed the
88 shape and propagation behavior of fatigue cracks.^{38,50–52} Microstructural alterations related to fatigue
89 crack initiation were also observed by diffraction contrast tomography (DCT) using ultrabright
90 synchrotron radiation X-rays.^{53,54} SR- μ CT has been applied to the observation of the RCF process;
91 however, the penetration depth of ultrabright synchrotron radiation X-rays is limited, so the sample
92 size should be less than 1 mm in all directions. Then samples should be cut from a bulk specimen to
93 include damaged areas. Stiénon et al. calculated the stress field around nonmetallic inclusions in
94 bearing steels in RCF tests using three-dimensional (3D) shapes obtained using SR- μ CT at the
95 European Synchrotron Radiation Facility (ESRF).^{33,34} The authors used SR- μ CT at the synchrotron
96 facility SPring-8 (Super Photon ring-8 GeV) to observe specimens exhibiting RCF-induced cracks,
97 and 3D imaging of the damage before flaking. To observe RCF damage before flaking, a circular hole
98 with a diameter of 15, 30, or 50 μ m and a depth of 50 to 200 μ m was formed in the specimen by
99 electrodischarge machining to investigate the effect of the shape of inclusions on crack initiation,
100 where the artificial hole simulates a stringer-type inclusion. Since the use of the artificial hole enabled
101 us to restrict the damaged area, the crack initiation and propagation from the hole before flaking could
102 easily to be observed.²⁴ To observe RCF damage, samples for SR- μ CT were cut out from this
103 specimen. It was found that many horizontal cracks started forming from the hole and were arranged
104 at almost equal distances before flaking. Lateral cracks were also formed; however, it was not clear
105 which was first, horizontal or lateral crack formation.

106 The mechanism of RCF crack initiation and propagation was discussed referring to the results
107 obtained by SR- μ CT and FE analysis.^{24,55–57} The introduction of the circular hole led to higher tensile
108 residual stress than that in the same region without the hole. In the case of a 15- μ m-diameter hole,
109 the RCF life, decreased with increasing hole length. On the other hand, in the case of a hole 50 μ m
110 in diameter, the hole length does not affect RCF life.

111 For successive SR- μ CT imaging of the RCF process, specimens must be sufficiently small to allow
112 the transmission of X-rays. We employed a specimen with a cross-sectional area of 500 μ m \times 500
113 μ m;³⁵ however, the mechanism of RCF in a thin specimen is different from that in a bulk specimen,
114 *i.e.*, the specimen broke without flaking. Therefore, synchrotron radiation computed laminography
115 (SR- μ CL) was employed, which allows the high-resolution, nondestructive imaging of thin plates
116 and hence successive observations of the RCF process leading to flaking with a specimen 1.0 mm
117 thick, 10 mm wide, and 24 mm long including vertical MnS inclusions.³⁵ It was found that lateral
118 cracks started forming from the inclusions first. After the formation of a lateral crack, the horizontal
119 crack was formed from the lateral crack and propagated leading to flaking. To elucidate the effects
120 of the orientation of stringer-type inclusions, RCF tests of a specimen with transverse inclusions were

conducted,^{36,37,58} the RCF mechanism was found to be similar to that in a specimen with vertical inclusions.

In the present study, RCF tests of specimens with longitudinal inclusions were conducted, and nondestructive successive observations of RCF crack initiation and propagation were accomplished by SR- μ CL for the first time. The results of these tests were compared with those obtained for specimens containing inclusions with transverse and vertical orientation, those published by the authors in previous papers^{36,37,58} to obtain the basic data for designing the optimum shape of inclusions. In these experiments, a model material with large stringer-type MnS inclusions was employed because inclusions in commercial bearing steel are too small to observe by SR- μ CL. Elastic FE analysis was conducted to clarify the differences in the crack initiation mechanism and mechanics in specimens with lateral inclusions, where the lateral inclusions include both transverse and vertical inclusions. The difference in fracture probability depending on inclusion orientation was also discussed. Vertical and transverse inclusions exist in mass-produced thrust and radial bearings, respectively, whereas longitudinal inclusions appear in large wrought bearings.

2 EXPERIMENTAL PROCEDURES

The material was the same bearing steel (modified JIS SUJ2) as that in a previous study,³⁶ whose chemical composition (in mass %) was as follows: 1.01 C, 0.33 Si, 0.45 Mn, 0.003 P, 0.049 S, and 1.50 Cr, with Fe making up the balance. The steel was not a commercial bearing steel, but it was fabricated in our laboratory to intentionally contain a high concentration of sulfur to enable the observation of crack initiation from stringer-type MnS inclusions. The deteriorative effect of MnS inclusion on RCF was reported for steel bearings.^{26,28,59} The steel was forged from an ingot with a diameter of 70 mm, and inclusions had preferential alignment along the forging direction. After the spheroidizing annealing of cementite particles, specimens were cut from the forged bar to obtain the inclusion orientation, as shown in Figure 1. The dimensions of the specimen for SR- μ CL imaging were 10 mm in width, 24 mm in length, and 1 mm in thickness. The thickness of the specimen was determined to allow the transmission of X-rays with sufficient intensity for imaging.³⁶ The specimen

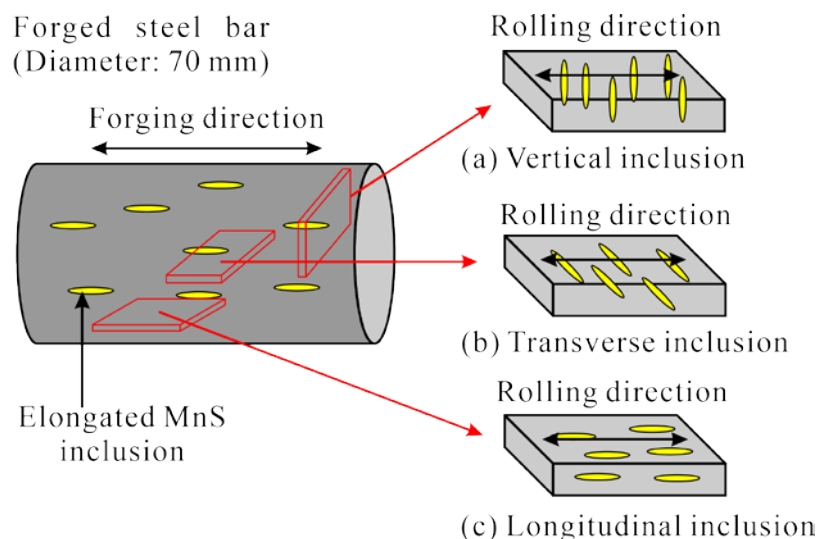


Figure 1 Orientation of inclusions in specimens

147 was quenched at 1103 K for 0.5 h and tempered at 453 K for 2 h. The average dimensions of MnS
 148 inclusions were 28.2 μm in length and 12.0 μm in diameter. Although those are much larger than the
 149 inclusions containing in actual bearings, the flaking mechanism is considered to be similar because
 150 the stress concentration is similar for similar shape inclusions.⁵⁷ Specimens with an artificial hole with
 151 a diameter of 15 μm and a depth of 200 μm , which was introduced by electrodischarge machining
 152 and simulates a vertical inclusion, were employed only for a preliminary test for the comparison of
 153 crack propagation behavior between rotating contact and reciprocal contact; other specimens had no
 154 artificial hole.

155 To conduct the RCF test near the experimental hatch of beam lines of the synchrotron radiation
 156 facility, SPring-8 (Super Photon Ring 8 GeV), a special ball-on-disk RCF testing machine was
 157 developed, as schematically illustrated in Figure 2, in which an eccentric cam converts the rotary
 158 movement of the motor to the reciprocal movement of the linear stage, the vibroconverter detects
 159 flaking of the specimen, and the proximity sensor detects the edge of the linear stage to count the
 160 number of cycles. In contrast to the conventional RCF testing machine in which the specimen rolls
 161 in one direction, our specimen moves reciprocally. Since the distance between the center of rotation
 162 of the motor and the center of the cam was 1.5 mm, the sliding distance of the ball on the specimen
 163 was 3.0 mm. A ceramic ball with a diameter of 6.0 mm and Young's modulus of 300 GPa was
 164 employed, and the specimen was immersed in naphthenic lubricant oil with a kinetic viscosity of 8.46
 165 mm^2/s to eliminate friction force.³⁶ The tests were carried out with reciprocating contact, whereas only
 166 the preliminary test in rotating contact was carried out to compare these two test procedures for specimens
 167 with an artificial hole. In general, bearings are subjected contact stress lower than 2 GPa, the contact
 168 stresses of higher than 5 GPa were also employed for accelerated testing of RCF^{11, 26, 28, 32}, because the
 169 RCF mechanism for the contact stress higher than 5 GPa is considered to be similar with that lower than
 170 2 GPa. In the present paper, results for a maximum Hertz stress, p_{max} , of 5.39 GPa are discussed. Since
 171 only 48 h was allowed for the use of the beam line of the synchrotron radiation facility every six
 172 months, the value of p_{max} was selected such that the RCF life was less than 48 h. RCF tests were

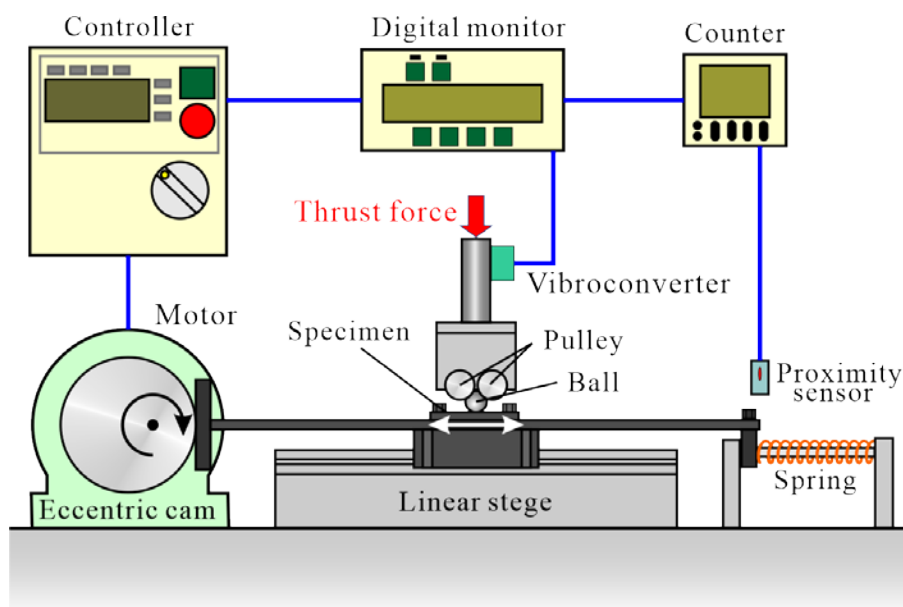


Figure 2 Rolling contact fatigue testing machine for laminography.

interrupted to conduct optical microscopy and SR- μ CL imaging to observe the crack initiation and propagation behaviors. SR- μ CL imaging was carried out at an undulator beam line of SPring-8. The experimental setup and the 3D reconstruction procedure are given elsewhere.³⁶

3 Experimental Results

3.1 Comparison of RCF behaviors between reciprocal and rotating testers

Since the rolling direction of bearings is usually only one way but is reciprocal in the present study, the crack propagation behaviors in the two methods are compared. Since the RCF life is probabilistic, depending on the scatter of inclusion size and shape, an artificial hole with a diameter of 15 μ m and depth of 200 μ m was formed in specimens by electrodischarge machining to simulate a vertical inclusion and to reduce the scatter. Figure 3 shows the appearance of the surface around the hole at $N=1.00\times 10^6$ cycles, indicating no significant difference in initial crack morphology. Figure 4 shows the propagation behavior of the crack at the surface, where the results of using reciprocal and rotating testers were obtained on two and three specimens, respectively. No significant difference was observed in the crack propagation behavior and RCF life, although the flaking occurred as a result of

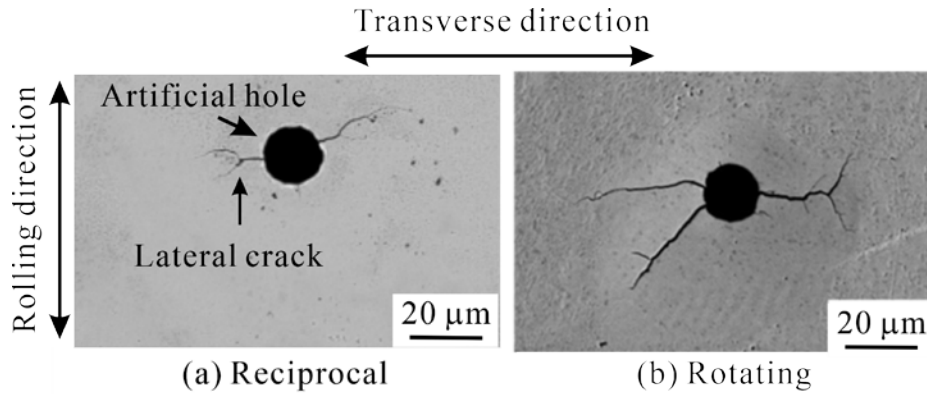


Figure 3 Lateral cracks emanating from artificial hole simulating vertical inclusion at $N = 1.00\times 10^6$ cycles.

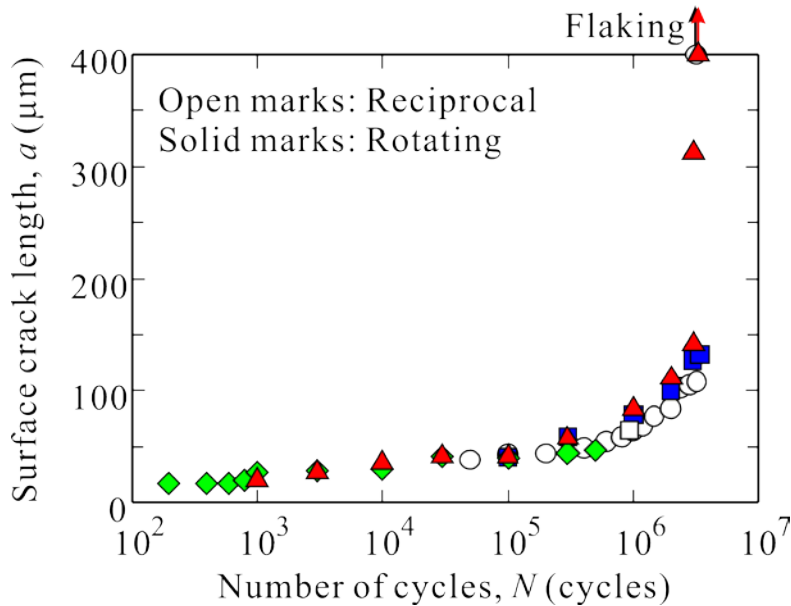


Figure 4 Propagation behavior of lateral cracks emanating from artificial hole.

the propagation of the horizontal crack beneath the surface, which was not observed from the surface. Therefore, the propagation behavior of the horizontal crack must also be similar for the two cases.

Since the morphology of lateral cracks emanating from inclusions are similar between vertical and transverse inclusions, the propagation behavior and RCF life in reciprocal and rotating RCF tests are considered to be similar.³⁷ They must also be similar for cracks in specimens with longitudinal inclusions because they are determined by the stress field far from the inclusions.

3.2 Optical microscopy at surface

Even though inclusions also exist beneath the surface, laminographies described in 3.3 showed that RCF cracks always first start forming from inclusions at the surface. Then, the crack initiation and propagation behaviors at the same site of the specimen surface were observed successively by optical microscopy; the results are shown in Figures 5 (Case I) and 6 (Case II). Longitudinal cracks started forming at the longitudinal ends of MnS inclusions, where the stress concentration is the highest, and propagated toward the rolling direction. Cracks have never been seen to form from other types of inclusion such as Al_2O_3 and TiN because the concentrations of these compounds are below the detection limit and the size of such inclusions are smaller than that of MnS inclusions.

As shown in Figure 5 (e), one tip of a longitudinal crack kinked to form a lateral crack when its length reached 90 μm . Figure 6 (d) indicates that both tips of the longitudinal crack kinked when the length of the longitudinal crack reached 129 μm , indicating that the kinking occurred almost simultaneously at both tips, except in the case shown in Figure 5 (e). Therefore, the kinking occurred when the length of the longitudinal crack reached approximately 100 μm regardless of the size of the inclusions where longitudinal cracks started to form. After the kinking, the lateral crack propagated

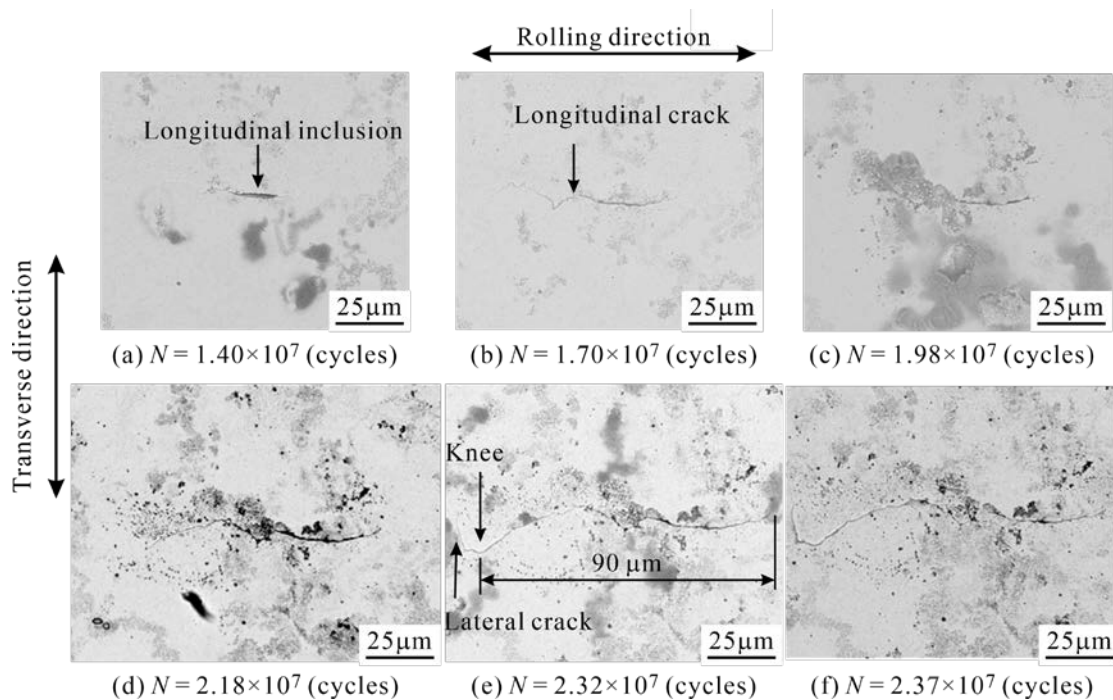


Figure 5 Crack initiation and propagation at surface observed by optical microscopy (Case I).

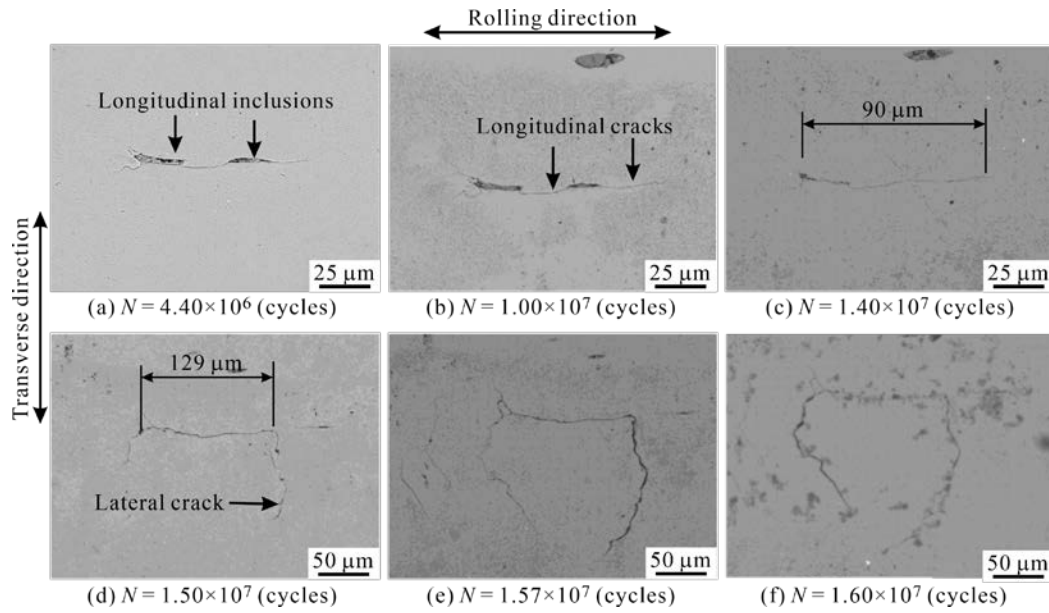


Figure 6 Crack initiation and propagation at surface observed by optical microscopy (Case II).

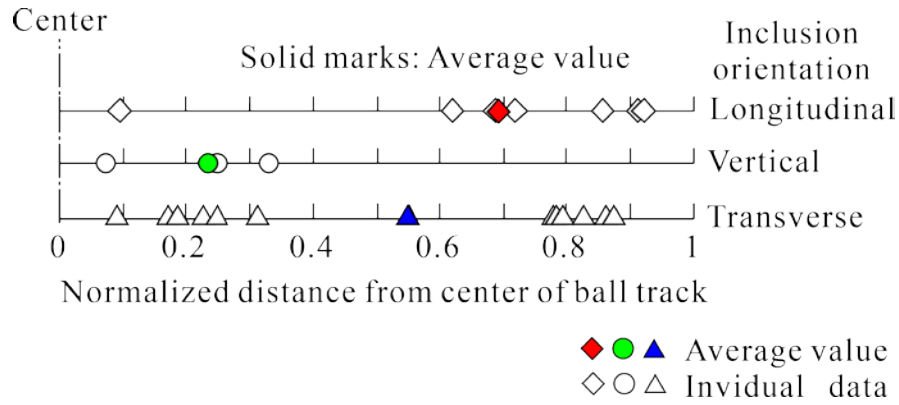


Figure 7 Distance between crack initiation site and center line of ball track, where distance was normalized by ball track width.

toward the transverse direction without the propagation of longitudinal cracks towards the rolling direction.

Figure 7 shows the crack initiation site in the ball track, where the distance along the transverse direction from the center of the ball track is normalized by half the ball track width. These values are the site for the initiation of the longitudinal crack for specimens with longitudinal inclusions, and the site for the formation of the lateral crack for specimens with transverse and vertical inclusions. Although the scatter is large, the average distance of the crack initiation site of specimens with longitudinal inclusions is close to the edge of the ball track, and close to the center line of ball track for specimen with vertical inclusions.

3.3 Laminography

3D SR- μ CL images of inclusions and cracks are shown from Figures 8 to 10, where (A) and (B) are the top and side views, respectively. In these images, dissimilar objects were indicated by colors depending on their depth from the surface; however, cracks and inclusions cannot be distinguished automatically in each SR- μ CT imaging process. Then, inclusions were identified as objects that did

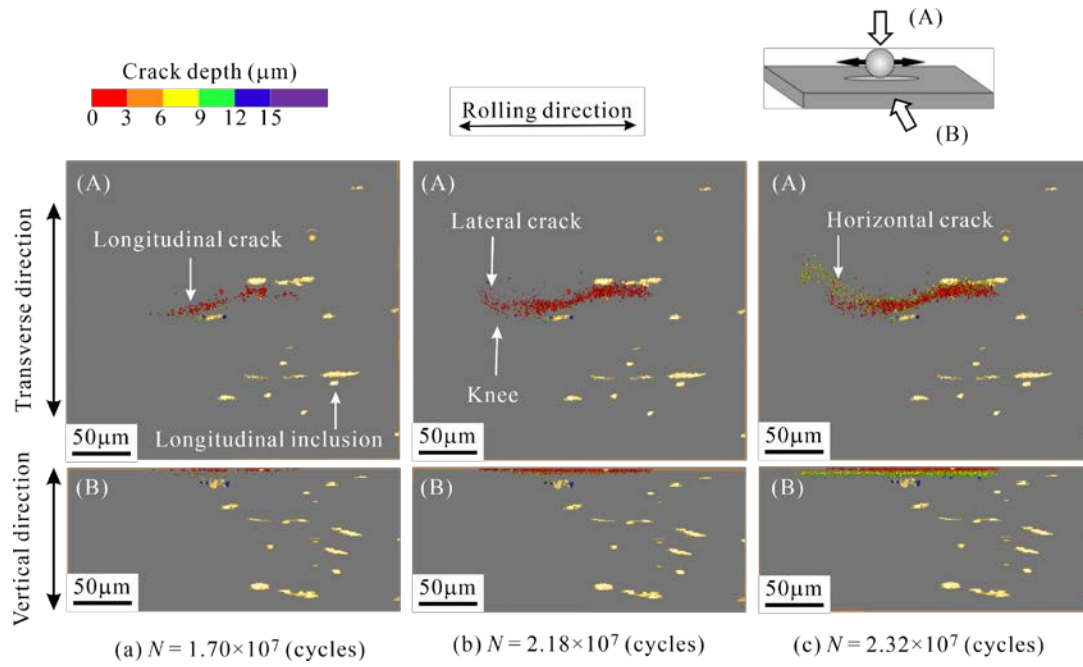


Figure 8 Laminography showing crack initiation from inclusion and propagation in sample with longitudinal inclusion, where color code indicates distance from sample surface (Case I).

Upper and lower figures show views from upper and side, respectively.

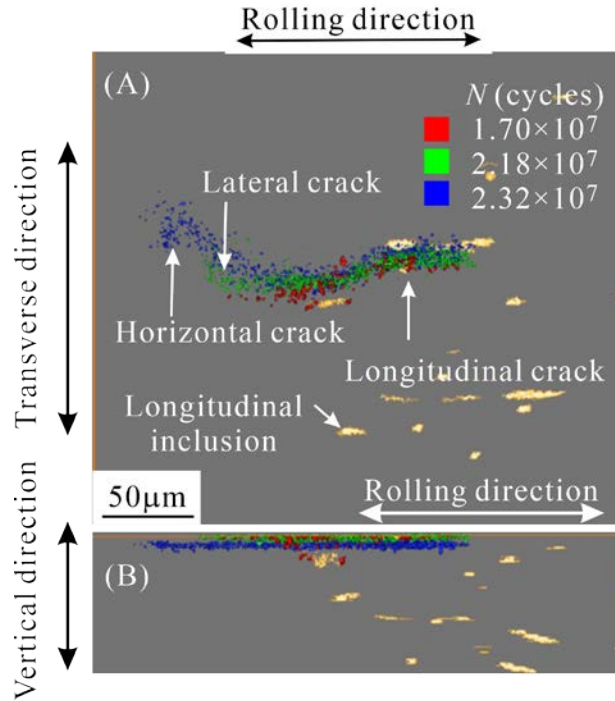


Figure 9 Laminography showing crack initiation from inclusion and propagation in sample with longitudinal inclusion, where color code indicates number of cycles at each observation (Case I).

Upper and lower figures show views from upper and side, respectively.

not change their shape or size in every observation, and they are indicated in pale yellow in the figures regardless of their location. However, the locations of inclusions changed after flaking because of the large plastic deformation of the specimen. Inclusions and cracks could not be distinguished, and both are indicated in color depending on their depth in Figure 10 (c).

Figure 8 (Case I) was obtained from the same specimen as that shown in Figure 5, where (a), (b), and (c) correspond to the optical micrographs in Figures 5 (b), (d), and (e), respectively. The kinking

of the longitudinal crack can be recognized in Figure 8 (b), although it was not observed in the optical micrograph obtained at the same number of cycles (2.18×10^7 cycles) as shown in Figure 5 (d). Figure 8 (c) indicates that the horizontal crack formed from the bottom of the lateral crack. Figure 9 shows the same crack (Case I), where each color indicates images obtained at each number of cycles. The formation sequence of the longitudinal, lateral, and horizontal cracks is clearly shown in this figure.

Another example of the flaking process is shown in Figure 10 (Case III), where two cracks are recognized, named Crack 1 and Crack 2. As shown in Figure 10 (a), the horizontal crack was already formed at the bottom of the lateral crack at the time of the first observation of Crack 1. After that, the horizontal crack propagated in both the rolling and transverse directions, as shown in Figure 10 (b), and further propagated to cause flaking, as shown in Figure 10 (c), where white arrows shown in (b) and (c) indicate the same position. The other crack, Crack 2, was also formed along an inclusion, but it remained a longitudinal crack.

4 Discussion

4.1 Flaking process

The following flaking process for specimens with a lateral inclusion was reported in our previous paper.³⁷ (1) A lateral crack is formed from an inclusion. (2) The crack propagates toward the lateral direction. (3) After the lateral crack propagates to a critical depth, a horizontal crack is formed from the lateral cracks. (4) The horizontal crack propagates under the surface to cause flaking. As described in the previous section, the flaking process for specimens with longitudinal inclusions was different. In this specimen, a longitudinal crack is formed first and propagates until it reaches a critical length. After the formation of the lateral crack, the RCF process for the specimen with longitudinal inclusions is similar to that of specimens with lateral inclusions. The formation of a longitudinal crack is an additional process for specimens with longitudinal inclusions. These processes are different from that previously proposed, in which the flaking starts from inclusions beneath the surface where the ball

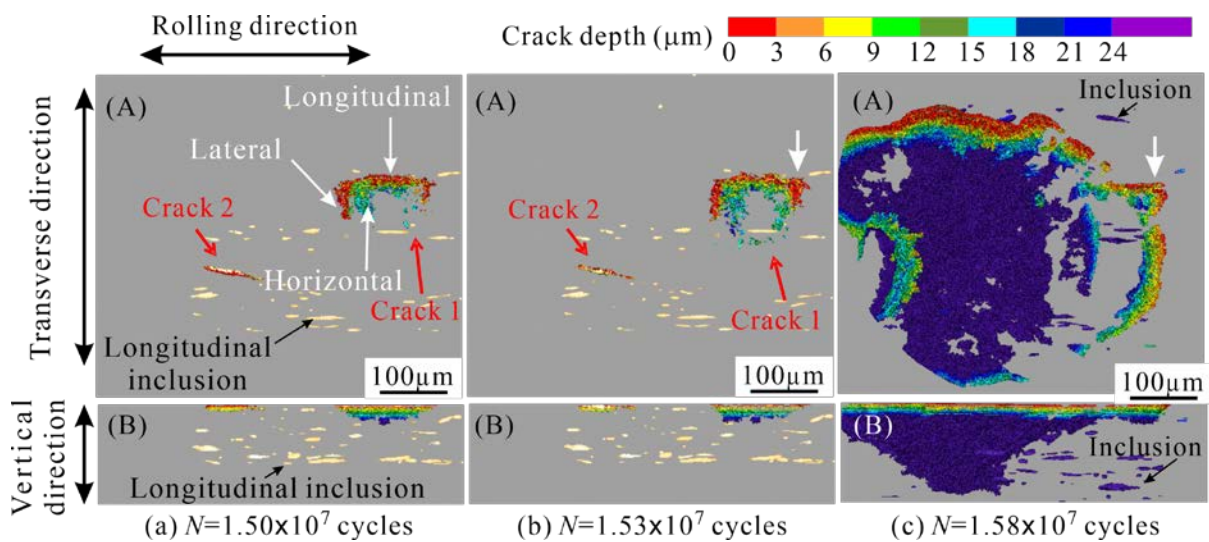


Figure 10 Laminography showing crack initiation from inclusion and propagation in sample with longitudinal inclusion, where color code indicates distance from sample surface (Case III). Upper and lower figures show views from upper and side, respectively.

track is located and the orthogonal shear stress is greatest, and the cracks grow from them to the surface.^{39,40}

For specimens with longitudinal inclusions, the number of cycles of longitudinal crack initiation was between 1.40×10^7 and 1.70×10^7 for Case I (Figure 5) and between 4.40×10^6 and 1.00×10^7 for Case II (Figure 6). The number of cycles of lateral crack initiation was between 1.98×10^7 and 2.18×10^7 for Case I (Figures 5 and 8) and between 1.40×10^7 and 1.50×10^7 for Case II (Figure 6). The number of cycles for crack initiation and flaking of the specimens will be described in 4.3.

4.2 Stress analysis

Since the effect of inclusion orientation on the RCF process is controlled by the stress field of matrix at the location of inclusions,^{5,42} and it can be approximated by that of an isolated inclusion in the matrix when the volume fraction of inclusions is low. The stress field of a homogeneous material induced by the contact with a spherical ball is axisymmetric about the normal of the contact surface, passing through the center of the contact ball. Under such an axisymmetric stress field, inclusions located at the same distance from the axis of symmetry and oriented to the same angle relative to the radial direction, are subjected to similar stress defined by the polar coordinate system. Consider two sites as inclusion locations, Points A and B, whose distance from the axis of symmetry is the same, as shown in Figure 11. The stress field defined by the polar coordinate system is similar between Points A and B. When the specimen moves along the x -axis (rolling direction), a stringer-type inclusion at Point A, whose longitudinal direction is perpendicular to the x -axis, is a transverse inclusion, whereas a stringer-type inclusion at Point B, whose longitudinal direction is parallel to the x -axis, is a longitudinal inclusion. For an inclusion at Point A (transverse inclusion), the change in the stress components with the movement of the specimen toward the rolling direction is equivalent to their change along the x -axis, whereas for the inclusion at Point B (longitudinal inclusion), their change is along the x' -axis, which is parallel to the x -axis.

When the transverse inclusion moves from Point A to C, all stress components defined by the polar coordinate system fixed to the ball are similar, whereas the antiplane shear stress component defined

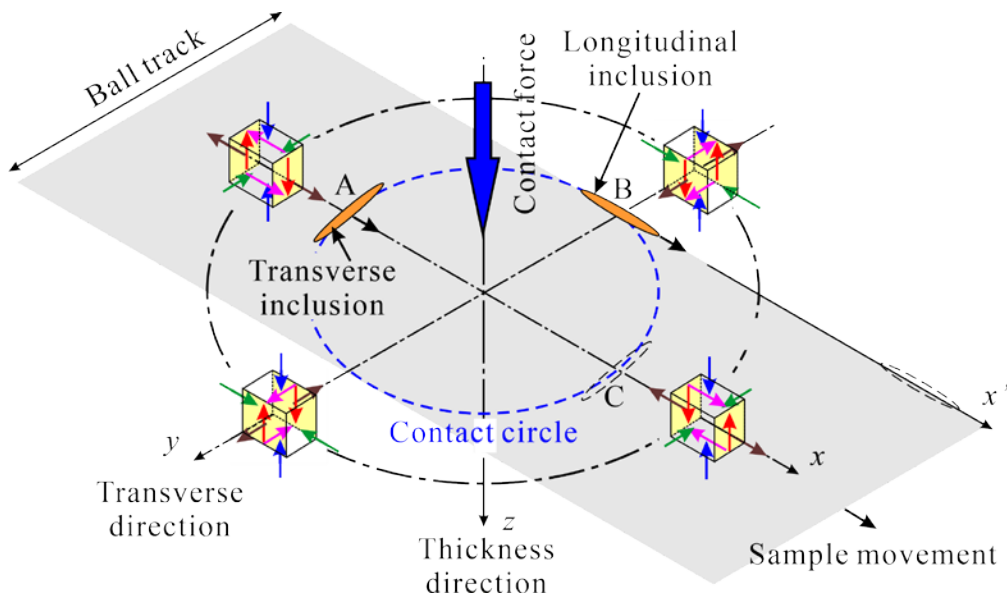


Figure 11 Schematic illustration of axisymmetric stress field due to contact force.

278 by the Cartesian coordinate system fixed to the specimen acts in opposite directions. Stress
279 components fixed to the specimen, except the antiplane shear stress, are similar at Points A and B,
280 indicating that the antiplane shear stress is alternating and other stress components are pulsating
281 during one pass of the contact ball. For the transverse inclusion located at Point B, each stress
282 component fixed to the specimen, including antiplane shear stress, are pulsating and take maximum
283 values at Point B in each pass of the contact ball. Therefore, the amplitude of the antiplane shear
284 stress acting on the transverse inclusion is twice that acting on the longitudinal inclusion, whereas the
285 amplitudes of other stress components are pulsating either for transverse and longitudinal inclusion.
286 The antiplane shear stress acting on a longitudinal inclusion at Point A is also alternating; however,
287 the stress concentration of this inclusion is significantly smaller than that of a longitudinal inclusion
288 at Point B. The stress concentration of a longitudinal inclusion at Point B is the same as that of a
289 transverse inclusion at Point A. Then, the difference in crack initiation behaviors between transverse
290 and longitudinal inclusions can be explained by the difference in the amplitude of antiplane shear
291 stress acting on these inclusions. In the case of a vertical inclusions at Point A, the stress is alternating,
292 whereas that is pulsating at Point B. Therefore, cracks start formation at Point A.

293 To confirm the above idea and the change in the antiplane shear stress due to the contact force, FE
294 analysis was conducted for the matrix, and the stress components defined by the Cartesian coordinate
295 system were calculated. ABAQUS Ver. 6.12 was used for the FE analysis. Although the elastic–
296 plastic analysis is required for a precise analysis, the 3D elastic FE analysis was conducted because
297 Makino et al. found through elastic–plastic FE analysis of RCF for specimens with artificial hole
298 which simulate the vertical inclusion, that plastic strain appears only during the initial few cycles
299 because of elastic shakedown.⁵⁵ They also showed that the shape of the stress distribution is almost
300 independent of the length of the hole, and is almost the same as that without a hole, while the peak
301 stresses depend on the length of the hole. The difference in peak stress for transverse and lateral
302 inclusions at the contact circle must be the same because they are mechanically equivalent under
303 axisymmetric loading.

304 The FE model consisted of a rectangular block and a hemisphere, and symmetry was considered
305 in the analysis.²⁴ The length, width, and height of the blocks were 20 mm, 6 mm, and 6 mm,
306 respectively, where infinite elements as defined in ABAQUS were applied in the region shown in
307 Figure 12. The length, width, and height of the solid element region were 10 mm, 3 mm, and 3 mm,
308 respectively. Therefore, accurate analysis was possible with a small number of elements. The actual
309 number of elements was 118,828 for the rectangular model and 32,914 for the hemispherical model.
310 Hertz stress of 5.22 GPa, Young’s modulus of 205.8 GPa, and Poisson’s ratio of 0.3. The radius of
311 the contact circle was 0.346 mm. In the previous paper employing similar FE analysis,²⁴ the
312 distribution of contact pressure obtained by FE analysis was calculated and compared with the
313 distribution obtained by Hertzian theory. No significant difference was found between them,
314 indicating that the FE model could simulate the contact condition assumed by the Hertzian theory.

315 Since the experimental results show that RCF cracks always start at the surface and the antiplane
316 shear stress is considered to be the driving force of crack initiation, the distribution of the antiplane
317 shear stresses at the surface calculated by the FE analysis is shown in Figure 12, where the antiplane
318 shear stresses τ_{xz} and τ_{yz} act on the plane normal to the rolling direction for specimens with lateral

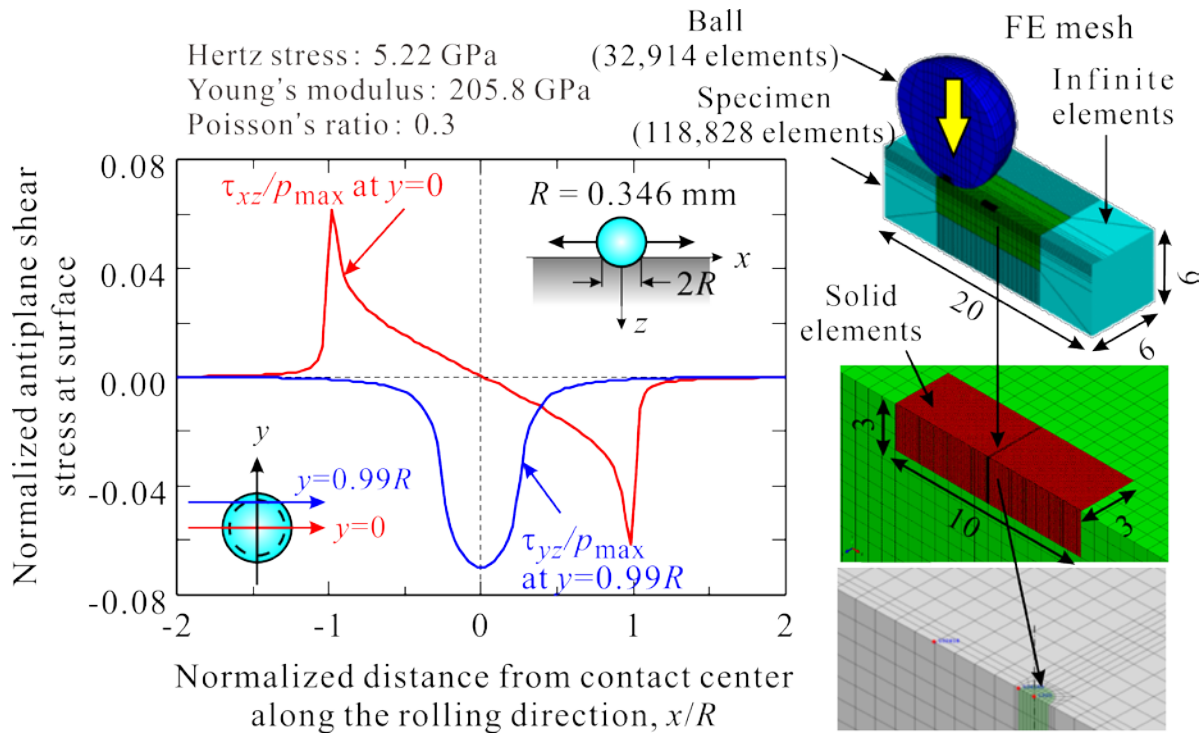


Figure 12 Distribution of antiplane shear stress at surface.

(transverse/vertical) inclusions and on the plane normal to the lateral direction for specimen with longitudinal inclusions, respectively. The distributions of τ_{xz} and τ_{yz} are along the center of the ball track ($y = 0$) and just inside of the ball track edge ($y = 0.99R$), respectively, where $R (= 0.346 \text{ mm})$ is the radius of the contact circle, *i.e.*, the half-width of the ball track. These values are maximum along the contact circle. Theoretically, the maximum values of τ_{xz} and τ_{yz} should be the same; however, the calculated $\tau_{xz,\max}$ is slightly smaller than $\tau_{yz,\max}$ because it is truncated owing to the rapid change in $\tau_{xz,\max}$ along the contact circle, where the calculated shear stresses depend on the mesh size of the FE analysis. Figure 12 is equivalent to the time variation of the stress components in the Cartesian coordinate system fixed to an inclusion (in other words, the specimen), where the abscissa axis represents time. The time variation of stress components during each motion of the specimen indicates that τ_{xz} is alternating and τ_{yz} is pulsating. These results of the FE analysis confirm that the supposition that the axisymmetric stress field is due to ball contact is appropriate. Again, this result indicates that the difference in the crack growth direction between specimens with lateral and longitudinal inclusions can be explained by considering the movement of inclusions fixed to the specimen, *i.e.*, the lateral inclusion receives an alternating cyclic stress, whereas the longitudinal inclusion receives a pulsating stress. Since the maximum stress is the same, the stress amplitude in the case of a longitudinal inclusion is half that in the case of a lateral inclusion.

Because of the stress concentration due to inclusions, RCF cracks start to form at the tips of inclusions; however, the stress amplitude in specimens with longitudinal inclusions is half that for specimens with lateral inclusions as mentioned above. This is why the crack initiation life for specimens with longitudinal inclusions is significantly longer than that for specimens with lateral inclusions. Owing to the long crack initiation life of specimens with longitudinal inclusions, inclusions originally located at the surface disappeared because of wear at the ball track. This seldom

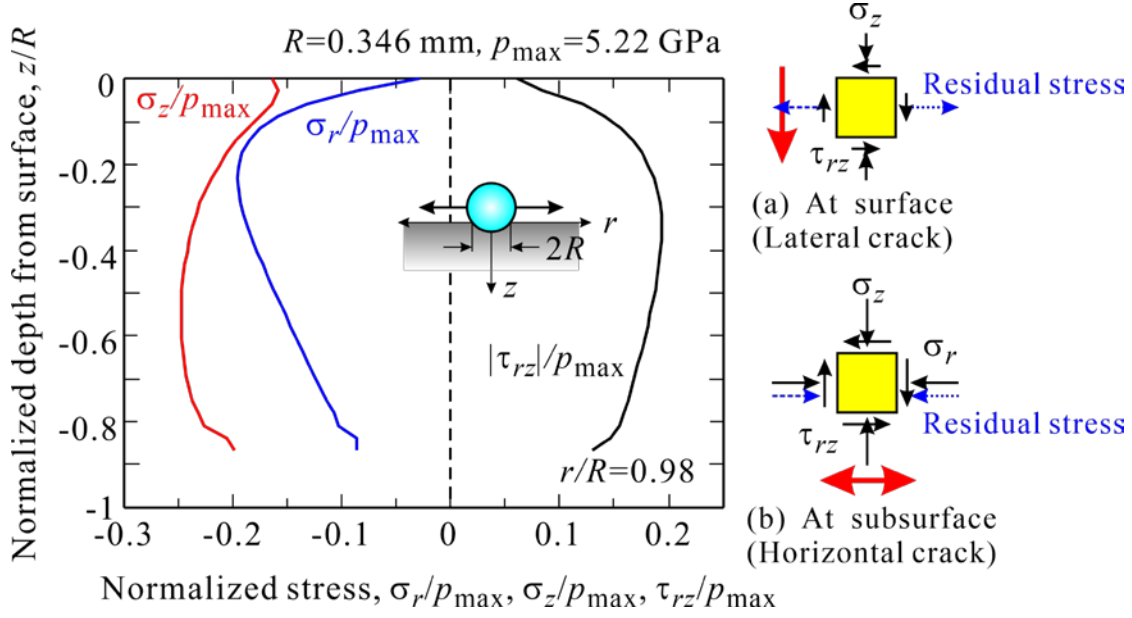


Figure 13 Stress distribution due to contact stress in depth direction.

happened with lateral inclusions. Then, inclusions beneath the surface appeared at the new surface, and cracks started to form from such inclusions. Small stress amplitude and wear synergetically elongate the crack initiation life of specimens with longitudinal inclusions.

Since the antiplane shear stress at the surface is maximum along the contact circle shown in Figure 12, RCF cracks in specimens with lateral inclusions tend to start forming at the center of the ball track, whereas the initiation site tends to be along the edge of the ball track for specimens with longitudinal inclusions, where the ball track is an envelope of the contact circle. This is consistent with the experimental results shown in Figure 7.

As shown in Figures 5 and 6, the kinking of the longitudinal crack occurred at almost the same crack length under comparable Hertz stress, and the kinking occurred almost simultaneously at both tips of a longitudinal crack, indicating that kinking is governed by the critical value of a mechanical factor such as the stress intensity factor, not a microstructural or metallurgical factor.

Contrary to the previously proposed mechanism that flaking starts from inclusions beneath the surface^{39,40}, the present experimental results showed that the horizontal crack formed after the formation of a lateral crack started forming at the surface. Therefore, the mechanics of flaking should be reconsidered. It has been believed that crack initiation is controlled by the orthogonal shear stress acting on the plane parallel to the surface and that the initiation and propagation of a horizontal crack causes flaking; however, the shear stress has a conjugate component, acting on the plane perpendicular to the surface. Indeed, results of laminography indicate that the existence of a lateral crack triggered the formation of a horizontal crack. As long as the orthogonal shear stress is the driving force of lateral crack formation and propagation, the normal stress acting on the plane where the orthogonal shear stress acts must govern the crack propagation plane. The normal stress acting on the plane perpendicular to the surface is the radial stress, σ_r , which is σ_x for the lateral crack started to form from a lateral inclusion, σ_y for the longitudinal crack started to form from a longitudinal inclusion, and σ_z acting on the face of the horizontal crack for specimens with each type of inclusion.

367 To examine the normal stress, the distribution of these stress components in the depth direction at
 368 the edge of the contact circle is calculated by FE analysis and shown in Figure 13. Since, the location
 369 of the transition from lateral to horizontal cracks is independent of the existence of inclusions, 3D FE
 370 analysis for the matrix was conducted. Figure 13 indicates that σ_r vanishes at the surface, but σ_z is
 371 compressive everywhere. According to the results of the elastic–plastic FE analysis conducted by
 372 Makino et al.,⁵⁵ the rolling-contact-induced residual stress in the radial direction is tensile at the
 373 surface, decreases in the depth direction, and changes to compressive some distance below the surface.
 374 Since the compressive stress acting on the crack face has a negative effect on crack propagation
 375 because of the friction acting on the crack plane, lateral crack initiation prevails over horizontal crack
 376 initiation near the surface; however, the antiplane shear stress decreases and the compressive residual
 377 stress acting on the plane increases with crack extension toward the depth direction. On the other
 378 hand, the conjugate shear stress and normal stress acting on the face of the horizontal crack is
 379 unchanged with crack extension as long as the horizontal crack propagates at the same depth.
 380 Therefore, near the surface, the lateral crack prevails over the horizontal crack, whereas the horizontal
 381 crack prevails some distance beneath the surface.

382 The authors have analyzed lateral and horizontal crack propagation behavior based on the fracture
 383 mechanics of an artificial hole.⁵⁵ Similar analysis must be better for more quantitative analysis;
 384 however, present analysis could confirm the stress analysis based on the axisymmetric stress field
 385 equivalent to Hertzian theory, and could explain the effect of inclusion orientation.

386 4.3 RCF life

387 Weibull plots of the RCF life are shown in Figure 14, and three-parameters in the Weibull plot and
 388 the average RCF life for each inclusion orientation are shown in Table 1. The smaller the shape

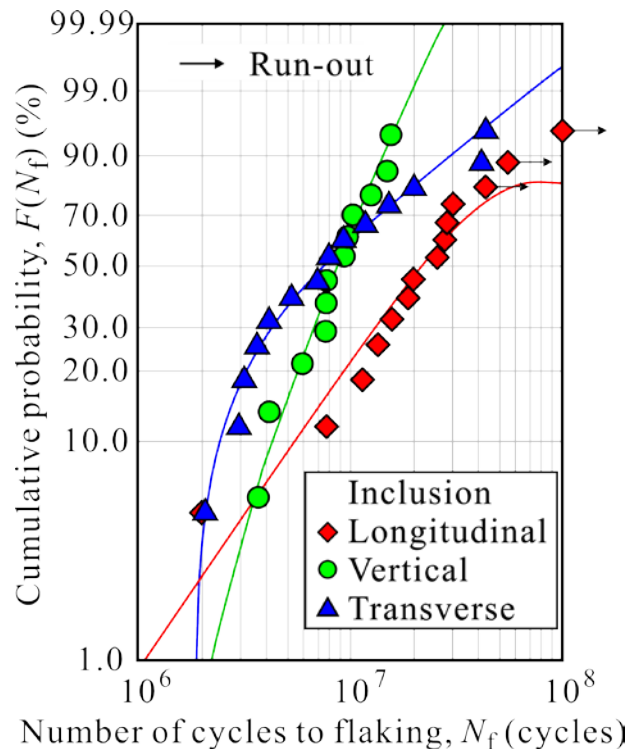


Figure 14 Weibull plot of rolling contact fatigue life.

Table 1 Effect of inclusion orientation on parameters in Weibull plot and average RCF life.

Inclusion orientation	Correlation	Number of samples, n	Shape parameter, α	Scale parameter, β	Location parameter, γ	Average RCF life (50 % fracture) (cycles)
Longitudinal	0.958	14	1.44	2.26×10^7	1.99×10^3	1.75×10^7
Vertical	0.984	12	2.08	8.95×10^6	1.23×10^6	8.74×10^6
Transverse	0.989	14	0.761	9.49×10^6	1.90×10^6	7.76×10^6

parameter, the more spread out the distribution,⁶⁰ and it is smallest for the specimen with vertical inclusions, indicating that the scatter of the diameter of inclusions is smaller than that of the length of inclusions because the RCF life is affected by the shape and size of the inclusion.

The average RCF life is almost the same for specimens with vertical and transverse inclusions. In contrast, Alley et al.⁴¹ estimated the effect of the orientation of the lateral inclusion on the RCF life, and concluded that the strength of the specimen with transverse inclusions is higher than that of the specimen with vertical inclusions due to the difference in stress concentration. Allison and Pandkar⁴² concluded that the RCF life of a specimen with longitudinal inclusions is almost the same as that of a specimen with transverse inclusions. Actually, the RCF life of a specimen with transverse inclusions is longer than that of a specimen with vertical inclusions in the long-life region ($F > 50\%$). Conversely, the former is shorter than the latter in the short-life region ($F < 50\%$). The RCF life of a specimen with longitudinal inclusions is always longer than that of a specimen with the lateral inclusions, indicating that the results of the FE analysis without considering the actual mechanism do not provide an accurate estimation.

Figure 15 shows plots of the lateral crack length, a , measured at the specimen surface against the number of cycles after crack initiation, $N - N_i$, where N_i is the lateral crack initiation life for specimens with the lateral inclusion and the longitudinal crack initiation life for specimens with the longitudinal

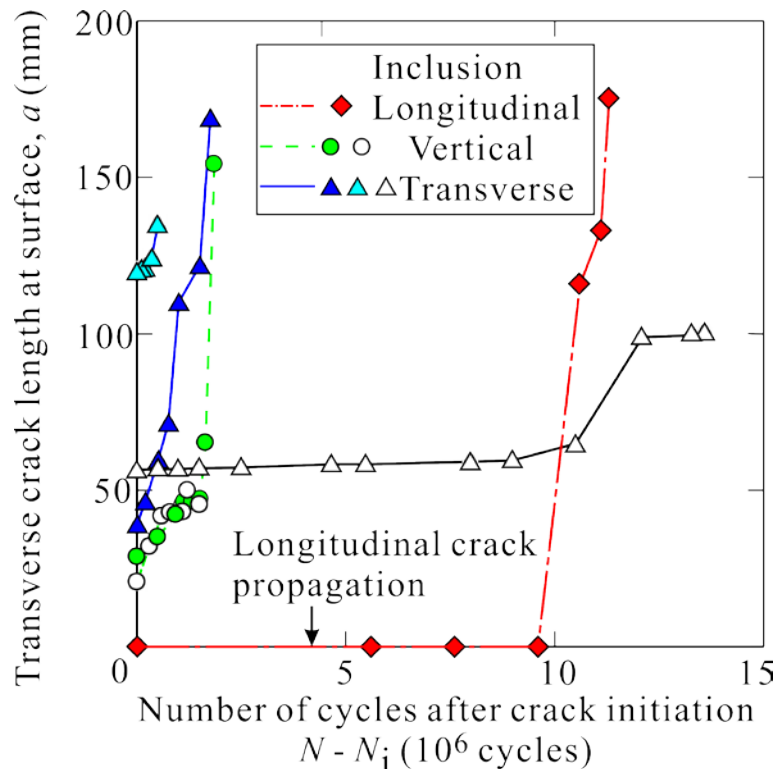


Figure 15 L-type crack propagation behavior observed at surface of specimen.

inclusion. Except data indicated by open triangles, for which flaking did not occur, the lateral crack propagation behaviors in specimens with longitudinal inclusions are similar to those in specimens with lateral inclusions.

To determine which process described in 4.1 is responsible for the difference in RCF life, the crack propagation life for each process was examined and shown in Figure 16, which shows the crack type observed at each number of cycles up to flaking. Except for one crack in a specimen with transverse inclusions that did not lead to flaking, the propagation lives of the lateral crack and the horizontal crack were similar for all types of specimen because cracks propagate far away from the initial inclusions. Therefore, the difference in RCF life depending on the orientation of inclusions should be attributed to the difference in the lateral crack initiation life. Therefore, the main difference in the RCF life for specimens with longitudinal inclusions compared with other specimens must originate from the longitudinal crack initiation and the propagation in the rolling direction.

5 CONCLUSIONS

In the present study, successive nondestructive 4D (3D imaging + time) observations of the formation and propagation of cracks in rolling contact fatigue (RCF) were performed on high-strength steel by synchrotron radiation computed laminography (SR- μ CL), and the crack path under RCF was discussed for specimens with stringer-type MnS inclusions elongated toward the rolling direction (longitudinal intrusion). The present results and those of previous RCF tests on specimens containing lateral (*i.e.*, transverse and vertical) inclusions were also compared. The following results were obtained.

1. Surface observation of the RCF process by optical microscopy showed that cracks were started forming from longitudinal inclusions. After propagation toward the rolling direction, the crack became kinked simultaneously at both tips of the longitudinal crack at the surface, and propagated toward the direction perpendicular to the rolling direction. The crack length at the time of kinking (the distance between knees $\approx 100 \mu\text{m}$) was almost independent of the length of the starter inclusion under comparable contact stress, indicating that the condition of kinking is determined by a mechanical factor.
2. Laminography of the RCF process showed that faces of cracks observed from the surface were vertical to the surface. After cracks reached a critical depth ($\approx 10 \mu\text{m}$), horizontal cracks were formed from the deepest point of the lateral crack, leading to flaking. The critical distance is thought to depend on the contact stress.
3. The formation of the longitudinal crack was the main difference in the RCF process of specimens with longitudinal inclusions, compared with that of specimens with lateral inclusions. Consequently, the RCF life of specimens with longitudinal inclusions was twice that of specimens with lateral inclusions. Not only mechanical factors but also wear is important in longitudinal crack initiation from longitudinal inclusions.
4. The effect of inclusion orientation on the crack path in RCF behavior could be explained in terms of antiplane shear stress acting on inclusions. Longitudinal inclusions received pulsated cyclic

stress, whereas the lateral inclusions received alternating cyclic stress. The antiplane shear stress amplitude of the former was half that of the latter. The formation of the horizontal crack was determined by the normal stress that acts on the orthogonal shear stress.

ACKNOWLEDGMENT

The synchrotron radiation experiments were performed at beam line BL46XU of SPring-8 with the approval of the Japan Synchrotron Radiation Research Institute (JASRI) under proposal numbers 2018A1548, 2018B1612, 2019A1635, 2019B1693, 2020A1620. The authors are grateful for the technical support of Dr. K. Kajiwarra (JASRI).

CONFLICT OF INTEREST

The authors declare that they have no conflict of interest.

AUTHOR CONTRIBUTIONS

Y. Nakai, D. Shiozawa, S. Kikuchi, T. Makino, and Y. Neishi conceived of the presented idea. T. Makino and Y. Neishi contributed to sample preparation. H. Saito, T. Nishina, and H. Kobayashi carried out the experiment. T. Makino performed the FE analysis. All authors contributed to the interpretation of the results. Y. Nakai, D. Shiozawa, S. Kikuchi, T. Makino, and Y. Neishi contributed to the final manuscript.

REFERENCES

1. Makino T, Kato T, Hirakawa K. The effect of slip ratio on the rolling contact fatigue property of railway wheel steel. *Int J Fatigue*. 2012;36:68-79.
2. Horimoto M, Makino T, Matsumoto H. The effect of slip conditions on the contact fatigue strength for pitting of a carburized steel. *Solid State Phenom*. 2006;118:521-526.
3. Meyler D, Magel E, Kalousek J. Reducing operating costs through improved wheel performance. 13th Int Wheelset Cong. 2001;CD-ROM.
4. Donzella G, Petrogalli C. A failure assessment diagram for components subjected to rolling contact loading. *Int J Fatigue*. 2010;32:256-268.
5. El Laithy M, Wang L, Harvey TJ, Vienneusel B. Further understanding of rolling contact fatigue in rolling element bearings-a review. *Tribology Int*. 2018;140:105849.
6. Šraml M, Flašker J, Potrč I. Numerical procedure for predicting the rolling contact fatigue crack initiation. *Int J Fatigue*. 2003;25:585-595.
7. Keer LM, Bryant MD. A pitting model for rolling contact fatigue. *J Lub Trib, Trans ASME*. 1983;105:198-205.
8. Hannes D, Alfredsson B. Rolling contact fatigue crack path prediction by the asperity point load mechanism. *Eng Fract Mech*. 2011;78:2848-2869.
9. Ringsberg JW, Loo-Morrey M, Josefson BL. Prediction of fatigue crack initiation for rolling contact fatigue. *Int J Fatigue*. 2000;22:205-215.

10. Ringsberg JW. Life prediction of rolling contact fatigue crack initiation. *Int J Fatigue*. 2001;23:575-586.
11. Ghaffari MA, Zhang Y, Xiao S. Multiscale modeling and simulation of rolling contact fatigue. *Int J Fatigue*. 2018;108:9-17.
12. Kanetani K, Ushioda K. Mechanism of white band (WB) formation due to rolling contact fatigue in carburized SAE4320 steel. *Mater Trans*. 2020;61:1750-1759.
13. Swahn H, Becker PC, Vingsbo O. Martensite decay during rolling contact fatigue in ball bearings. *Metallurg Trans*. 1976;7A:1099-1110.
14. Šmeļova V, Schwedt A, Wang L, Holweger W, Mayer J. Microstructural changes in white etching cracks (WECs) and their relationship with those in dark etching region (DER) and white etching bands (WEBs) due to rolling contact fatigue (RCF). *Int J Fatigue*. 2017;100:148-158.
15. Li S, Wu J, Petrov RH, Li Z, Dollevoet R, Sietsma J. "Brown etching layer": A possible new insight into the crack initiation of rolling contact fatigue in rail steels?. *Eng Fail Anal*. 2016;66:8-18.
16. Li SX, Su YS, Shu XD, Chen JJ. Microstructural evolution in bearing steel under rolling contact fatigue. *Wear*. 2017;380-381:146-153.
17. Evans MH, Walker JC, Ma C, Wang L, Wood RJK. A FIB/TEM study of butterfly crack formation and white etching area (WEA) microstructural changes under rolling contact fatigue in 100Cr6 bearing steel. *Mater Sci Eng: A*. 2013;570:127-134.
18. Su YS, Li SX, Yu F, Lu SY, Wang YG. Revealing the shear band origin of white etching area in rolling contact fatigue of bearing steel. *Int J Fatigue*. 2021;142:105929.
19. Grabulov A, Ziese U, Zandbergen HW. TEM/SEM investigation of microstructural changes within the white etching area under rolling contact fatigue and 3-D crack reconstruction by focused ion beam. *Scripta Mater*. 2007;57:635-638.
20. Hiraoka K, Nagao M, Isomoto T. Study on flaking process in bearings by white etching area generation. *ASTM STP 1465*. 2007;234-240.
21. Martin JA, Borgese SF, Eberhardt AD. Microstructural alterations of rolling bearing steel undergoing cyclic stressing. *J Basic Eng Trans ASME*. 1966;88:555-565.
22. Sugino K, Miyamoto K, Nagumo M, Aoko K. Structural alterations of bearing steels under rolling contact fatigue. *Trans ISIJ*. 1970;10:98-111.
23. Becker PC. Microstructural changes around non-metallic inclusions caused by rolling-contact fatigue of ball-bearing steels. *Metals Tech*. 1981;234-243.
24. Makino T, Neishi Y, Shiozawa D, Fukuda Y, Kajiwaru K, Nakai Y. Evaluation of rolling contact fatigue crack path in high strength steel with artificial defects. *Int J Fatigue*. 2014;68:168-177.
25. Chen Q, Shao E, Zhao D, Guo J, Fan Z. Measurement of the critical size of inclusions initiating contact fatigue cracks and its application in bearing steel. *Wear*. 1991;147:285-294.

26. Nagao M, Hiraoka K, Unigame Y. Influence of nonmetallic inclusion size on rolling contact fatigue life in bearing steel. Sanyo Tech Report. 2005;12:38-45.
27. Kerrigan A, Kuijpers JC, Gabelli A, Ioannides E. Cleanliness of bearing steels and fatigue life of rolling contacts. ASTM STP 1465. 2007;101-106.
28. Unigame Y, Hiraoka K, Takasu I, Kato Y. Evaluation procedures of nonmetallic inclusions in steel for highly reliable bearings. J ASTM Int. 2007;3:34-41.
29. Hashimoto K, Fujimatsu T, Tsunekage N, Hiraoka K, Kida K. Effect of inclusion/matrix interface cavities on internal-fracture-type rolling contact fatigue life. Mater Des. 2011;32:4980-4985.
30. Lewis MWJ, Tomkins B. A fracture mechanics interpretation of rolling bearing fatigue, proceedings of the institution of mechanical engineers, Part J. J Eng Tribol. 2012;226:389-405.
31. Neishi Y, Makino T, Matsui N, Matsumoto H, Higashida M, Ambai H. Influence of the inclusion shape on the rolling contact fatigue life of carburized steels. Metall Mater Trans A. 2013;44:2131-2139.
32. Tsuchida T, Tamura E. Mechanism of crack initiation at non-metallic inclusion under rolling contact fatigue in bearing steels. Kobe Steel Eng Reports. 2011;61:62-65.
33. Stiénon A, Fazekas A, Buffiere J-Y, Vincent A, Daguiet P, Merchi F. A new methodology based on X-ray micro-tomography to estimate stress concentrations around inclusions in high strength steels. Materials Sci Eng A. 2009;513-4:376-383.
34. Stiénon A, Fazekas A, Buffiere J-Y, Daguiet P, Merchi F, Vincent A. A new methodology for predicting fatigue properties of bearing steels: from X-ray micro-tomography and ultrasonic measurements to the bearing lives distribution. J ASTM Int. 2010;7:1-14.
35. Shiozawa D, Makino T, Neishi Y, Nakai Y. Observation of rolling contact fatigue cracks by laminography using ultra-bright synchrotron radiation. Procedia Mat Sci. 2014;3:159-164.
36. Nakai Y, Shiozawa D, Kikuchi S, Sato K, Obama T, Makino T, Neishi Y. In situ observation of rolling contact fatigue cracks by laminography using ultra-bright synchrotron radiation. Frattura Integ Stru. 2014;34:267-275.
37. Nakai Y, Shiozawa D, Kikuchi S, Obama T, Saito H, Makino T, Neishi Y. 4D observations of rolling contact fatigue processes by laminography using ultra-bright synchrotron radiation. Eng Fract Mech. 2017;183:180-189.
38. Nakai Y, Shiozawa D, Kurimura T, Kajiwara K. Observation of fretting fatigue cracks by micro computed-tomography using ultrabright synchrotron radiation. Proc SPIE. 2010;7522:75224B: 1-7.
39. Gustaf L, Palmgren A. Dynamic capacity of rolling bearings. J Appl Mech, Trans ASME. 1949;16:165-172.
40. Styri H. Fatigue strength of ball bearing races and heat-treated 52100 steel specimens. Proc ASTM. 1951;51:682-700.

41. Alley ES, Neu RW. Microstructure-sensitive modeling of rolling contact fatigue. *Int J Fatigue*. 2010;32:841-850.
42. Allison B, Pandkar A. Critical factors for determining a first estimate of fatigue limit of bearing steels under rolling contact fatigue. *Int J Fatigue*. 2018;117:396-406.
43. Shen Y, Mobasher S, Sadeghi MF, Paulson K, Trice RW. Effect of retained austenite – Compressive residual stresses on rolling contact fatigue life of carburized AISI 8620 steel. *Int J Fatigue*. 2015; 5:135-144.
44. Walvekar AA, Sadeghi F. Rolling contact fatigue of case carburized steels. *Int J Fatigue*. 2017;95:264-281.
45. Golmohammadi Z, Walvekar A, Sadeghi F. A 3D efficient finite element model to simulate rolling contact fatigue under high loading conditions. *Tribology Int*. 2018;126:258-269.
46. Zhao YX, Liu HB. Weibull modeling of the probabilistic S–N curves for rolling contact fatigue. *Int J Fatigue*. 2014;66:47-54.
47. Vijay A, Paulson N, Sadeghi F. A 3D finite element modelling of crystalline anisotropy in rolling contact fatigue. *Int J Fatigue*. 2018;106:92-102.
48. Naeimi M, Li Z, Qian Z, Zhou Y, Wu J, Petrov RH, Sietsma J, Dollevoet R. Reconstruction of the rolling contact fatigue cracks in rails using X-ray computed tomography. *NDT E Int*. 2017;92:199-212.
49. Jessop C, Ahlstrom J, Hammar L, Faster S. 3D characterization of rolling contact fatigue crack networks. *Wear*. 2016;366-7:392-400.
50. Shiozawa D, Nakai Y, Kurimura T, Morikage Y, Tanaka H, Okado H, Miyashita T, Kajiwaru K. Observation of cracks in steels using synchrotron radiation X-ray micro tomography. *J Soc Mater Sci Jpn*. 2007;56:951-957.
51. Yoshinaka F, Nakamura T, Nakayama S, Shiozawa D, Nakai Y, Uesugi K. Non-destructive observation of internal fatigue crack growth in Ti-6Al-4V by using synchrotron radiation μ CT imaging. *Int J Fatigue*. 2016;93:397-405.
52. Shiozawa D, Nakai Y, Murakami T, Noshio H. Observation of 3D shape and propagation mode transition of fatigue cracks in Ti-6Al-4V under cyclic torsion using CT imaging with ultra-bright synchrotron radiation. *Int J Fatigue*. 2014;58:158-165.
53. Shiozawa, D, Nakai, Y, Miura, R, Masada, N, Matsuda, S, Nakao, R, 4D evaluation of grain shape and fatigue damage of individual grains in polycrystalline alloys by diffraction contrast tomography using ultrabright synchrotron radiation, *Int J Fatigue*. 2016;82:247-255.
54. Nakai Y, Shiozawa D, Asakawa N, Nonaka K, Kikuchi S. Change of misorientation of individual grains in fatigue of polycrystalline alloys by diffraction contrast tomography using ultrabright synchrotron radiation. *Structural Integrity Procedia*. 2017;3:402-410.

55. Makino T, Neishi Y, Shiozawa D, Kikuchi S, Okada T, Kajiwara K, Nakai Y. Effect of defect shape on rolling contact fatigue crack initiation and propagation in high strength steel. *Int J Fatigue*. 2016;92:507-516.
56. Makino T, Neishi Y, Shiozawa D, Kikuchi S, Saito H, Kajiwara K, Nakai Y. Rolling contact fatigue damage from artificial defects and sulphide inclusions in high strength steel. *Procedia Struct Integ*. 2017;7:468-475.
57. Makino T, Neishi Y, Shiozawa D, Kikuchi S, Okada S, Kajiwara K, Nakai Y. Effect of defect length on rolling contact fatigue crack propagation in high strength steel. *Frattura Integ Stru*. 2015;34:379-386.
58. Nakai Y, Shiozawa D, Kikuchi S, Obama T, Saito H, Makino T, Neishi Y. Effects of inclusion size and orientation on rolling contact fatigue crack initiation observed by laminography using ultra-bright synchrotron radiation. *Procedia Struct Integ*. 2016;2:3117-3124.
59. Neishi Y, Makino T, Matsui N, Matsumoto H, Higashida M, Ambai H. Influence of Inclusion Shape on the Rolling Contact Fatigue Life of Carburized Steels, *Metallur Mater Trans*. 2013;44A:2013-2131.
60. Kikuchi S, Kubozono H, Nukui Y, Nakai Y, Ueno A, Kawabata MO, Ameyama K. Statistical fatigue properties and small fatigue crack propagation in bimodal harmonic structured Ti-6Al-4V alloy under four-point bending. *Mater Sci Eng A*. 2018;711:29-36.

List of Table and Figures

TABLE 1	Effect of inclusion orientation on parameters in Weibull plot and average RCF life.
FIGURE 1	Orientation of inclusions in specimens.
FIGURE 2	Rolling contact fatigue testing machine for laminography.
FIGURE 3	Lateral cracks emanating from artificial hole simulating inclusion at $N = 1.00 \times 10^6$ cycles.
FIGURE 4	Propagation behavior of lateral cracks emanating from artificial hole.
FIGURE 5	Crack initiation and propagation at surface observed by optical microscopy (Case I).
FIGURE 6	Crack initiation and propagation at surface observed by optical microscopy (Case II).
FIGURE 7	Distance between crack initiation site and center line of ball track, where distance was normalized by half of ball track width.
FIGURE 8	Laminography showing crack initiation from inclusion and propagation for specimen with the longitudinal inclusion, where color code indicates distance from specimen surface (Case I). Upper and lower figures show views from upper and side, respectively.
FIGURE 9	Laminography showing crack initiation from inclusion and propagation for specimen with the longitudinal inclusion, where color code indicates number of cycles at each observation (Case I). Upper and lower figures show views from upper and side, respectively.
FIGURE 10	Laminography showing crack initiation from inclusion and propagation for specimen with the longitudinal inclusion, where color code indicates distance from specimen surface (Case III). Upper and lower figures show views from upper and side, respectively.
FIGURE 11	Schematic illustration of axisymmetric stress field due to contact force.
FIGURE 12	Distribution of antiplane shear stress at surface.
FIGURE 13	Stress distribution due to contact stress in the depth direction.
FIGURE 14	Weibull plot of rolling contact fatigue life.
FIGURE 15	Lateral crack propagation behavior observed at surface of specimen.
FIGURE 16	Number of cycles for crack propagation where N_f is number of cycles to flaking for flaking specimen, and final number of cycles for specimen without flaking.